Supplementary Figure Legends

Figure S1. Visualize the four OPA1 tetramers used in MD and provide an overview of the setup of MD simulations. (A-C) Three tetrameric subassemblies of the S-OPA1 polymer (tetramers 2, 3, and 4) were fitted into the corresponding density map that is transparently visible. Each monomer is shown in surface representation and colored differently for clarity. Tetramer 2 **(A)** is extracted from the polymeric model in membrane-proximal conformation, while tetramers 3 **(B)** and 4 **(C)** are extracted from the polymeric model that represents the membrane-distal conformation of the S-OPA1 polymer. **(D, E)** Superimposition of the S-OPA1 tetramers assembled using different oligomerization interfaces. **(D)** Tetramers representing the conserved crisscross association of dynamin superfamily proteins. **(E)** The newly identified interface 7 mediates the formation of other tetrameric assemblies in the membrane-bound state. The root-mean-square deviation (RMSD) is calculated using the CLICK server. **(F)** A representative image of the membrane patch used CG MD simulations. The lipid molecules are shown in magenta (CL), green (POPC), and cyan (POPE) and the subunits of the S-OPA1 tetramer are colored blue, yellow, orange, and gray. The membrane-inserting loop (MIL) region is highlighted in green. S-OPA1 tetramers are positioned closely to the membrane patch in the simulations. After <1 μs simulation time, the tetramers rapidly formed charge-charge and hydrophobic interactions with the bilayer lipids and deformed the membrane patch. **(G)** The S-OPA1 tetramers containing mutations within the MIL and docking regions do not bind the membrane patch and remain in solution within the timescale of the simulations.

Figure S2. Sequence alignment of OPA1 paddle domain (PD) from various species. The sequence alignment of PD residues (736 to 860) demonstrates high sequence conservation across 33 species.

Figure S3. Membrane deformation analysis of S-OPA1 tetramer in CG MD simulations. Red and blue colors indicate membrane pulling and pushing in the direction of z, respectively. The x and y axes indicate the number of membrane tiles; each tile represents 15 Å. **(A)** Membrane deformation calculations are shown for two other independent replicas using S-OPA1 tetramer 1 and model membranes containing either 20% CL (left) or 20% MLCL (right). The membrane deformation activity of tetramer 1, particularly its ability to push down on the sides, is reduced in the presence of MLCL. **(B)** Average membrane deformation was calculated for S-OPA1 tetramers 2, 3, and 4. A comparison of CL- and MLCL-containing membranes indicates reduced membrane deformation in the presence of MLCL for tetramer 3. While the CG MD simulations with tetramers 1 and 3 display significant membrane bending with CL-containing membranes, tetramers 2 and 4 show no visible difference between the two membranes.

Figure S4. Membrane binding and remodeling experiments. (A) A representative size-exclusion chromatography (SEC) profile of S-OPA1 WT and **(B)** SDS-PAGE of S-OPA1 protein following SEC. **(C)** Membrane reconstitution assays of S-OPA1 WT using four different liposomes containing POPC, POPE, L-PI, and CL at various concentrations. The PC:PE:PI:CL liposomes contain 45% POPC, 22% POPE, 8% L-PI, and 25% CL; the PC:PE:PI liposomes contain 70% POPC, 22% POPE, and 8% L-PI; the PC:PE liposomes contains 78% POPC and 22% POPE; and the PC liposomes contain 100% POPC. The samples were incubated for ~4 hours at room temperature and visualized by using negative-stain TEM. Scale bar is 100 nm. **(D)** Co-sedimentation assays were performed with the same liposomes as in (C). Supernatant and pellet samples were collected after centrifugation, subjected to SDS-PAGE, and quantified using ImageJ. An unpaired two-tailed student T test was used for statistical analysis. The asterisk(s) above the bars indicate the following: $P<0.0001$ (****), $P<0.001$ to $P>0.0001$(***), $P<0.005$ to $P>0.001$ (**), $P<0.05$ to $P>0.005$(*), and $P>0.05$ (not significant, ns).

Figure S5. Validation of brominated cardiolipin. (A) Mass spectrum of brominated cardiolipin from 780 to 1280 mass to charge ratio (m/z). **(B)** Zoomed-in view of the mass spectrum from 1042 to 1052 m/z. **(C, D)** The brominated cardiolipin chemistry was validated by small ligand NMR. The NMR Spectrum of cardiolipin H^1 **(C)** and brominated cardiolipin H^1 **(D)**. **(E)** Representative negative-stain TEM images of reconstitution assays show cylindrical and spherical liposomes in the presence and absence of S-OPA1 WT. Protein samples bind and form higher-order assemblies on brominated and native liposomes. Scale bar is 100 nm.

Figure S6. CryoEM imaging and image analysis of S-OPA1 assemblies bound to brominated liposomes. (A) Electron cryo-micrograph showing S-OPA1 filaments assembled on liposomes containing CL-Br. **(B)** Representative 2D class averages of S-OPA1 filament segments. **(C)** Gold-standard Fourier Shell Correlation (FSC) curve of the final density map. **(D)** Local resolution estimates for the cryoEM 3D reconstruction. Both horizontal and vertical slices through cryo-EM densities are shown. **(E)** S-OPA1 tetramer bound to brominated nanotubes (colored) superimposed with the tetrameric model bound to native nanotubes (gray) show minimal structural differences between the two models.

Figure S7. CryoEM data processing flowchart of S-OPA1 bound to brominated cardiolipin containing membranes. Details of cryoEM data collection and image analysis are described in the methods section.

Figure S8. Comparison of the Coulombic potentials from the resulting 3D maps of unlabeled versus bromine labeled membrane tubes. (A) A gray scale slice of along the helical axis shows CL enrichment in the outer leaflet. **(B)** Radial profiles from the cryoEM 3D reconstructions indicate the location of the surplus signals attributed to halogen scattering. The red box in panel A indicates the region used in intensity analysis. **(C)** Zoomed in view of a horizontal slice through the cryo-EM density map showing S-OPA1 monomer-membrane interactions. Dashed circles indicate the regions used in intensity measurements. **(D)** Radial profile measurements for the protein-membrane contact sites indicate the location of the surplus signals attributable to halogen scattering near the MIL region. The delta intensity is calculated by using the cryoEM 3D reconstructions of native and brominated protein-bound lipid nanotubes. **(E)** A gray scale slice of the difference map of S-OPA1 polymer bound to native and brominated liposomes shows CL enrichment in the outer leaflet. IL, Inner Leaflet; OL, Outer Leaflet; PD, Paddle Domain.

Figure S9. Comparison of residence times for CL and MLCL lipids in AA and CG MD simulations. (A) Residence times for contacts between S-OPA1 residues and CL (blue line) and MLCL (red line) lipids in CG MD simulations. The data was averaged over four subunits in each tetramer and three replicas. **(B)** Average number of protein-lipid contacts calculated from three replicas of AA MD simulations using S-OPA1 tetramer and CL- and MLCL-enriched membranes.

Figure S10. Negative-stain TEM images of liposomes. Different molar concentrations of CL and MLCL were used to prepare various liposomes. Electron microscopy images show similar morphology for liposomes containing increasing concentrations of MLCL compared to CL-enriched liposomes. Scale bars are 100 nm.

Table S1. Cryo-EM data collection, refinement, and validation statistics for the two tetrameric S-OPA1 models.

Table S2. List of liposome compositions used in reconstitution assays, co-sedimentation experiments, and cryoEM imaging. (A) Lipid molar concentrations of individual lipids in CL-containing liposomes. **(B)** Lipid molar concentrations of individual lipids in CL- and MLCL-containing liposomes. **(C)** The lipid composition of liposomes and nanotubes containing brominated cardiolipin (CL-Br).

Figure S1

A

Tetramer 2

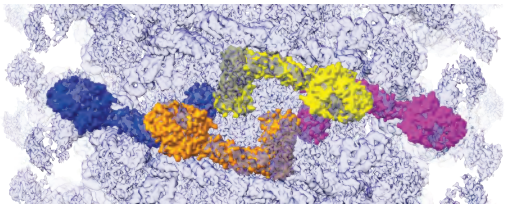

B

Tetramer 3

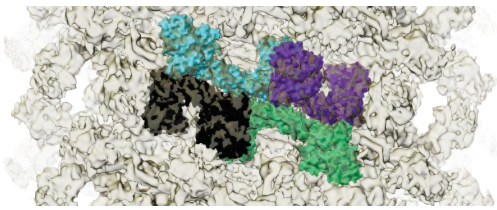

C

Tetramer 4

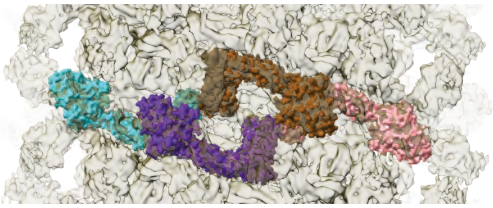

D

RMSD 2.49 Å

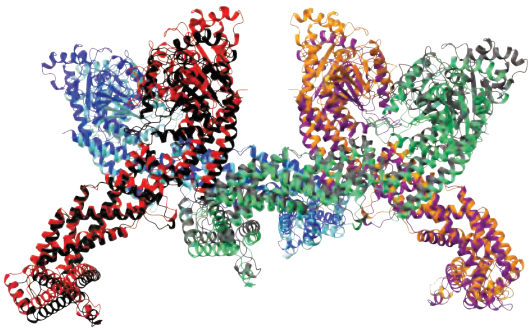

E

RMSD 2.47 Å

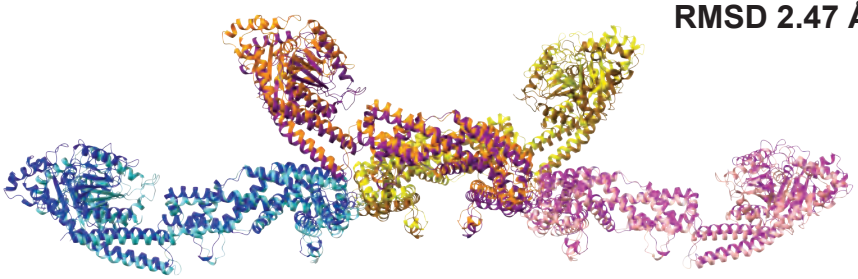

F

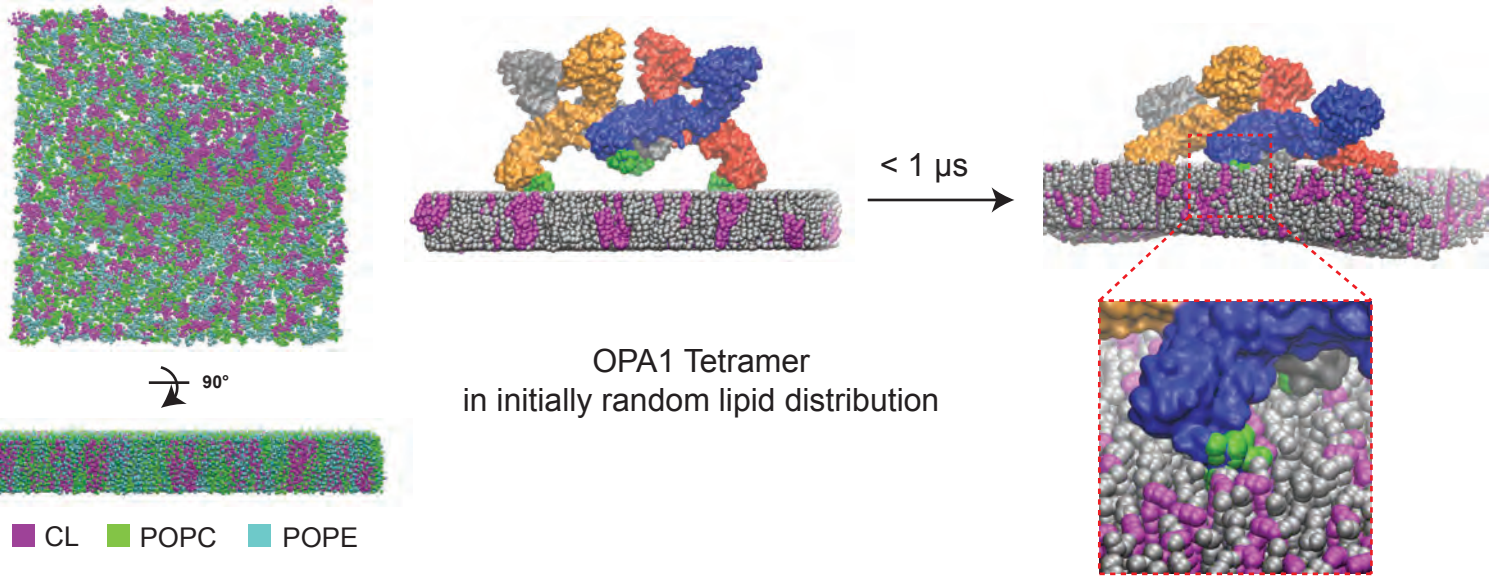

G

Mutant OPA1 Tetramer

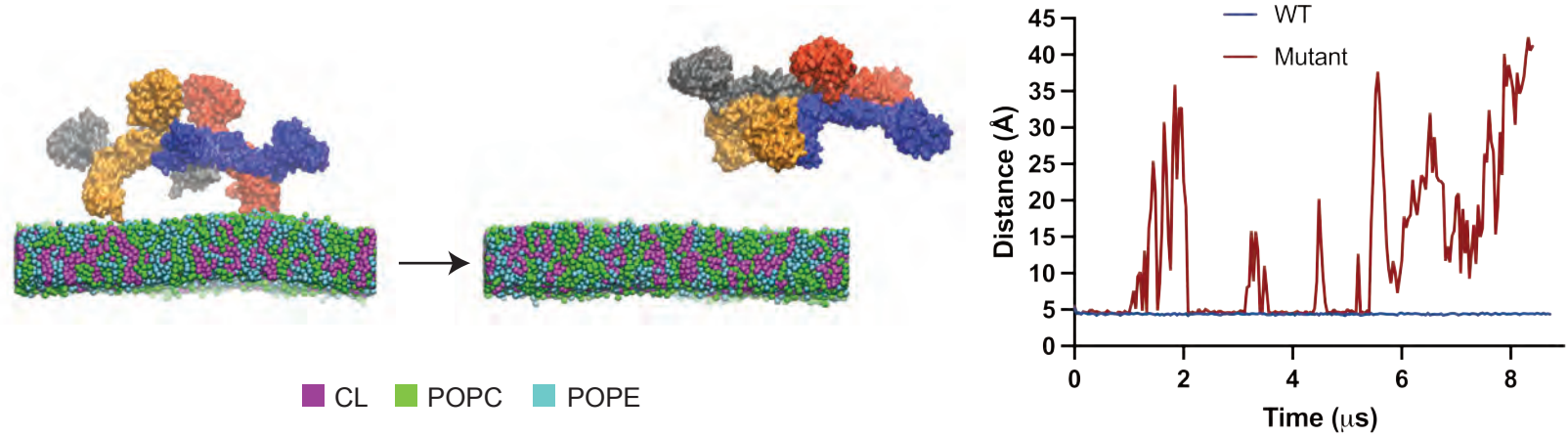

Figure S2

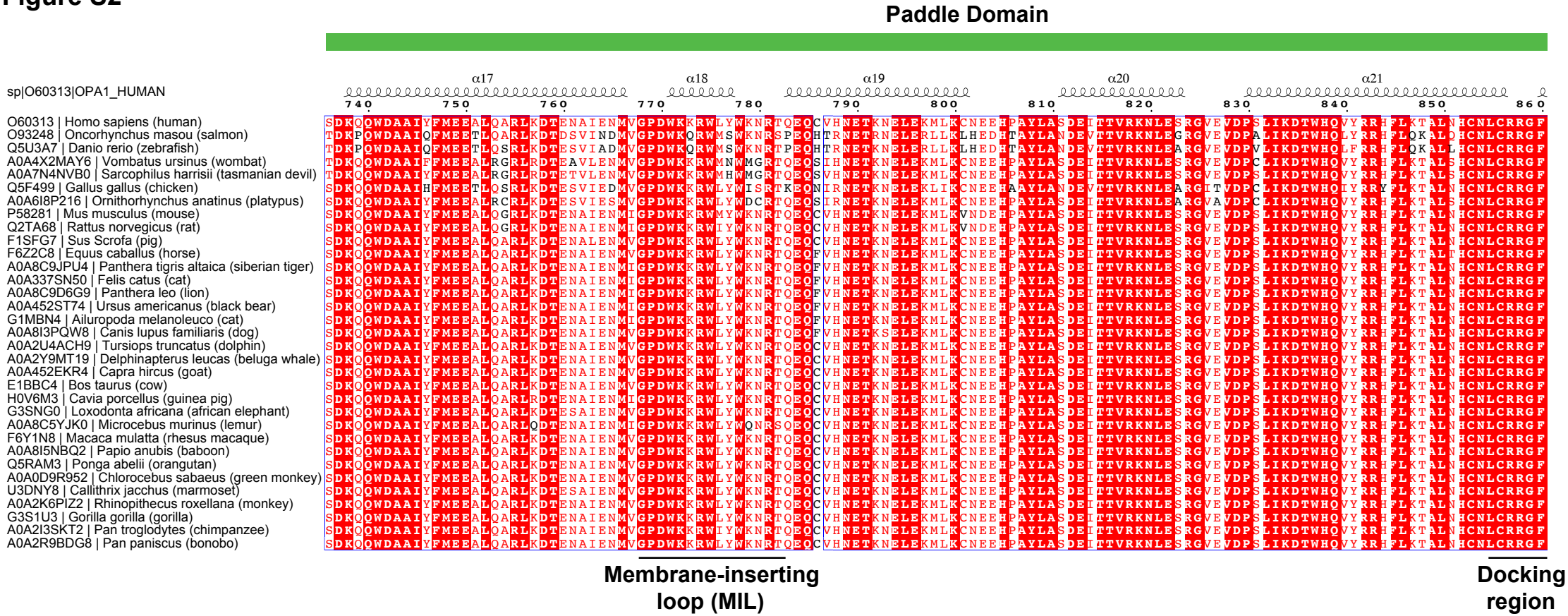
Paddle Domain
α17
α18
α19
α20
α21
sp|O60313|OPA1_HUMAN
740
750
760
770
780
790
800
810
820
830
840
850
860
O60313 | Homo sapiens (human)
O93248 | Oncorhynchus masou (salmon)
Q5U3A7 | Danio rerio (zebrafish)
A0A4X2MAY6 | Vombatus ursinus (wombat)
A0A7N4NVB0 | Sarcophilus harrisii (tasmanian devil)
Q5F499 | Gallus gallus (chicken)
A0A6I8P216 | Ornithorhynchus anatinus (platypus)
P58281 | Mus musculus (mouse)
Q2TA68 | Rattus norvegicus (rat)
F1SFG7 | Sus Scrofa (pig)
F6Z2C8 | Equus caballus (horse)
A0A8C9JPU4 | Panthera tigris altaica (siberian tiger)
A0A337SN50 | Felis catus (cat)
A0A8C9D6G9 | Panthera leo (lion)
A0A452ST74 | Ursus americanus (black bear)
G1MBN4 | Ailuropoda melanoleuco (cat)
A0A8I3PQW8 | Canis lupus familiaris (dog)
A0A2U4ACH9 | Tursiops truncatus (dolphin)
A0A2Y9MT19 | Delphinapterus leucas (beluga whale)
A0A452EKR4 | Capra hircus (goat)
E1BBC4 | Bos taurus (cow)
H0V6M3 | Cavia porcellus (guinea pig)
G3SNG0 | Loxodonta africana (african elephant)
A0A8C5YJK0 | Microcebus murinus (lemur)
F6Y1N8 | Macaca mulatta (rhesus macaque)
A0A8I5NBQ2 | Papio anubis (baboon)
Q5RAM3 | Ponga abelii (orangutan)
A0A0D9R952 | Chlorocebus sabaeus (green monkey)
U3DNY8 | Callithrix jacchus (marmoset)
A0A2K6PIZ2 | Rhinopithecus roxellana (monkey)
G3S1U3 | Gorilla gorilla (gorilla)
A0A2I3SKT2 | Pan troglodytes (chimpanzee)
A0A2R9BDG8 | Pan paniscus (bonobo)
Membrane-inserting loop (MIL)
Docking region

Figure S3

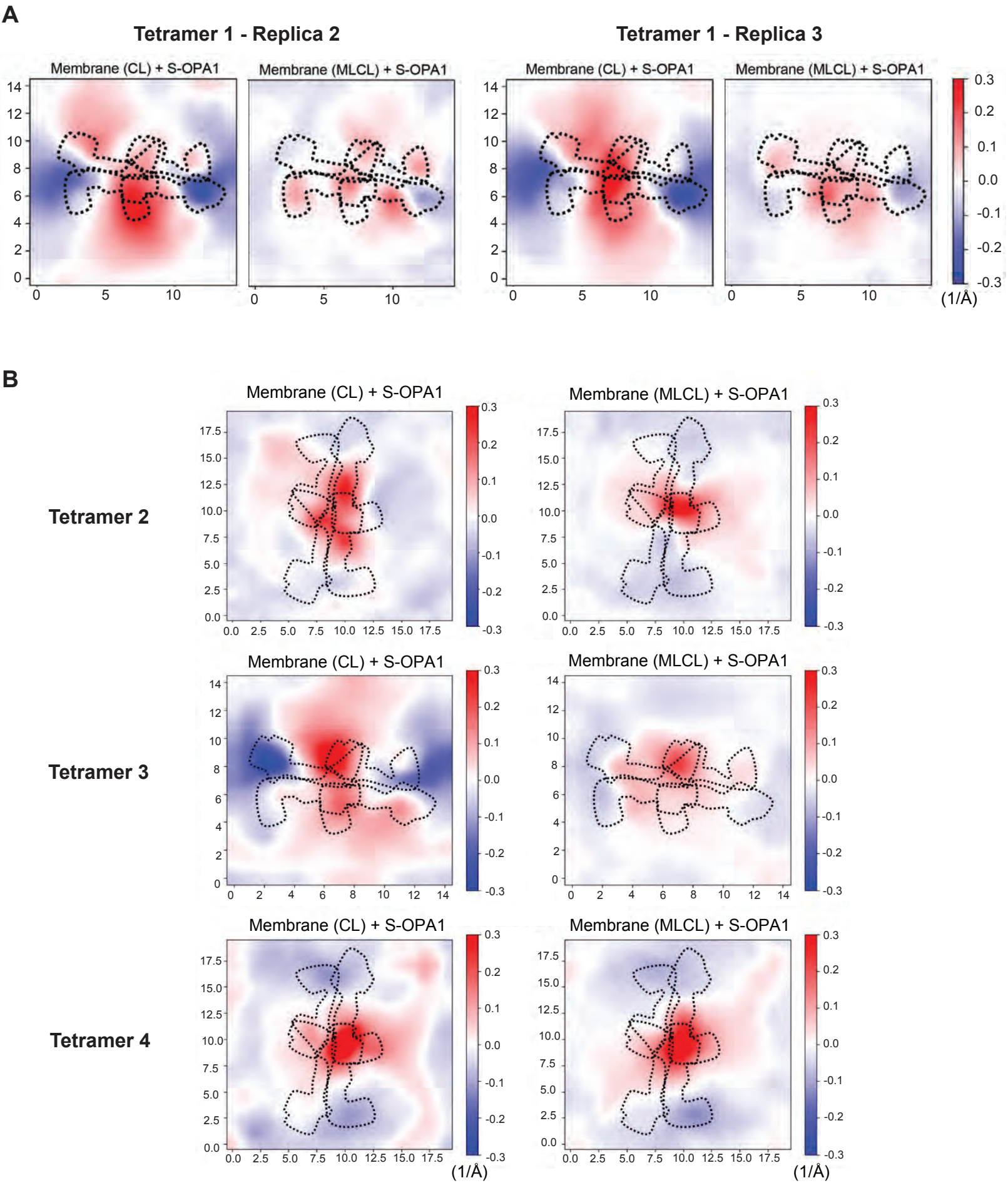

Figure S4

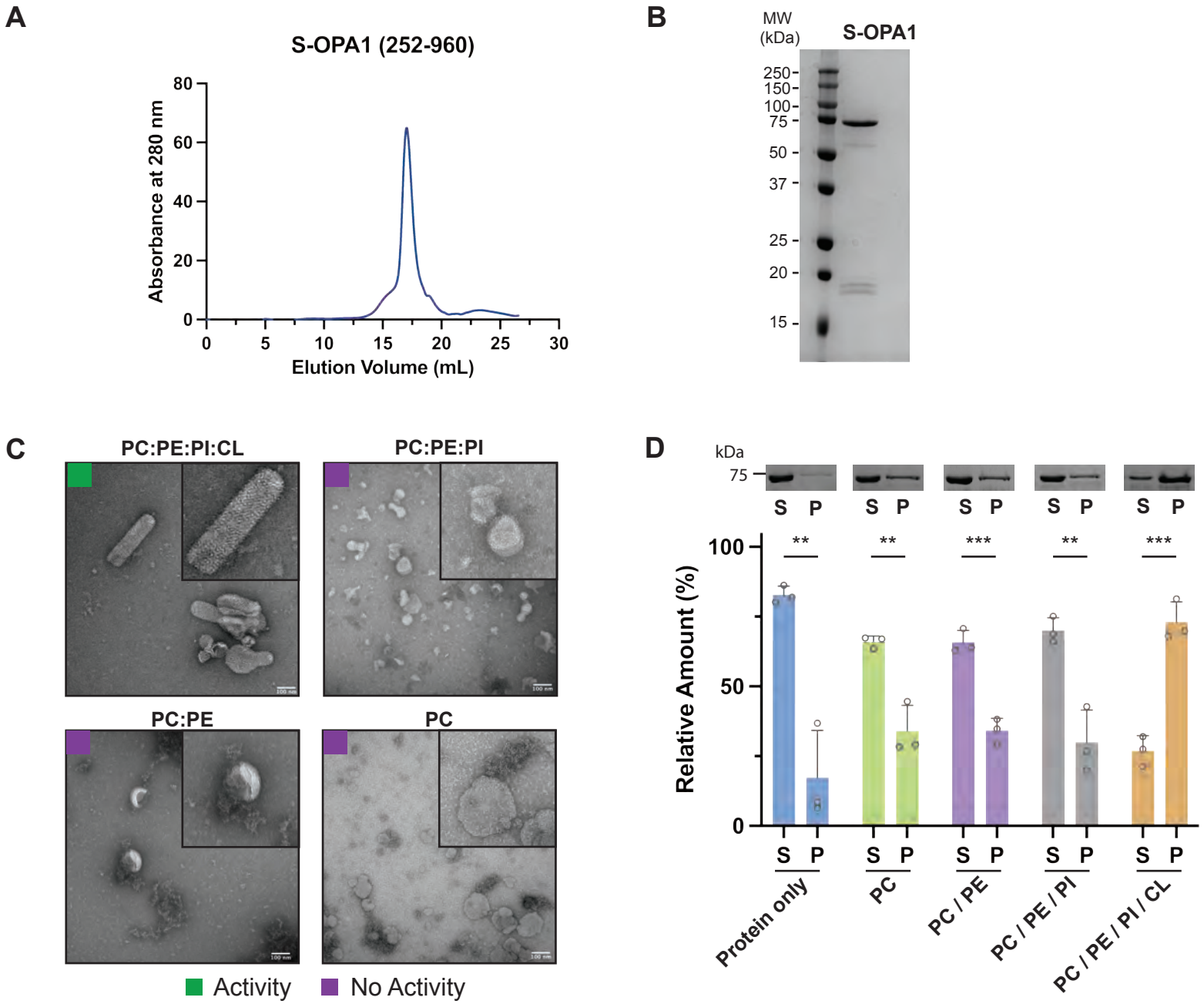

Figure S5

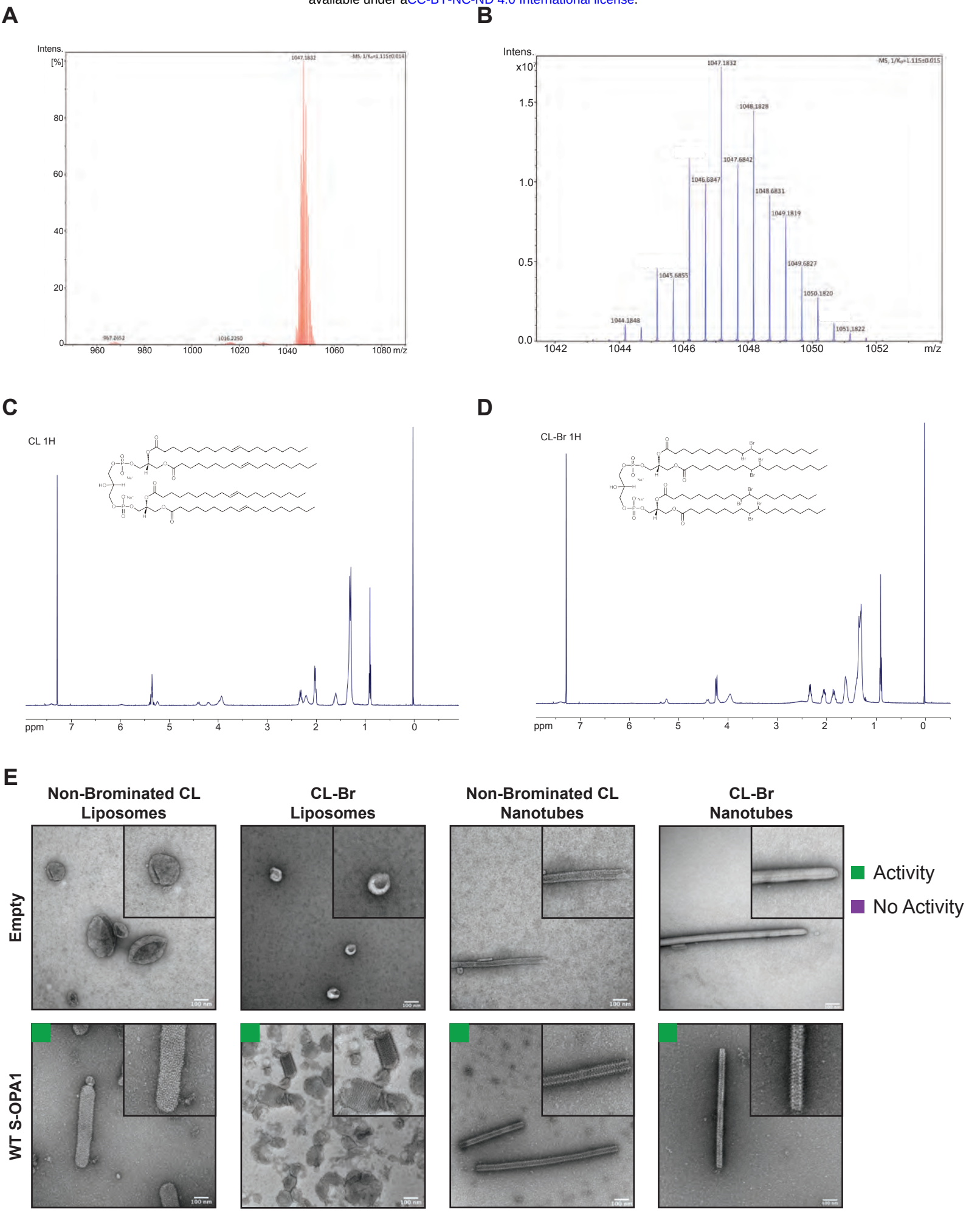

Figure S6

A

B

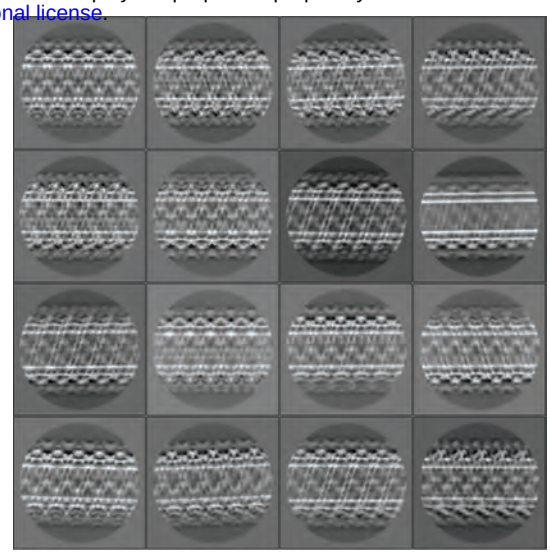

C

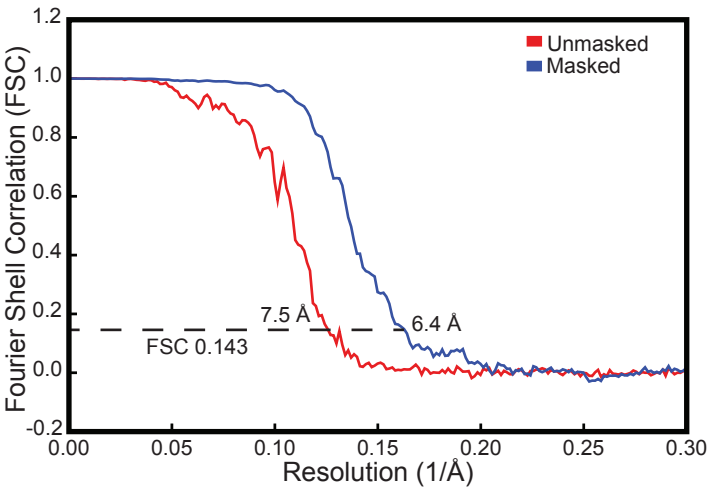

D

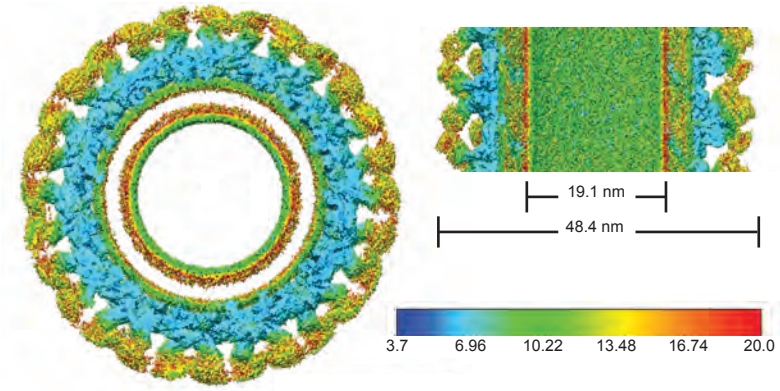

E

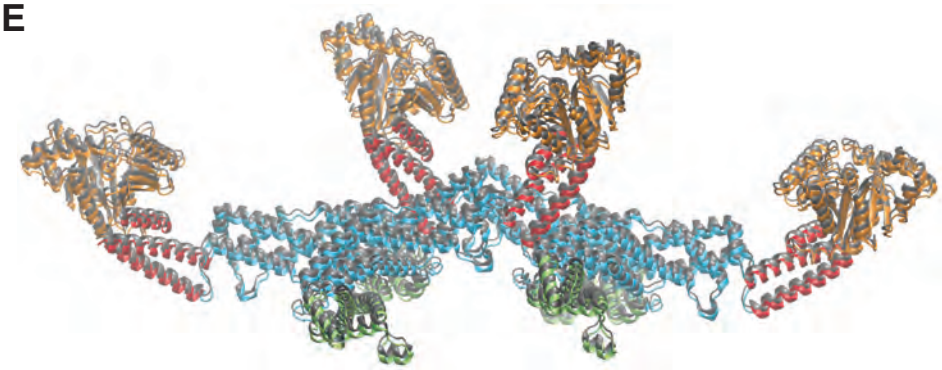

0.78Å RMSD

Figure S7

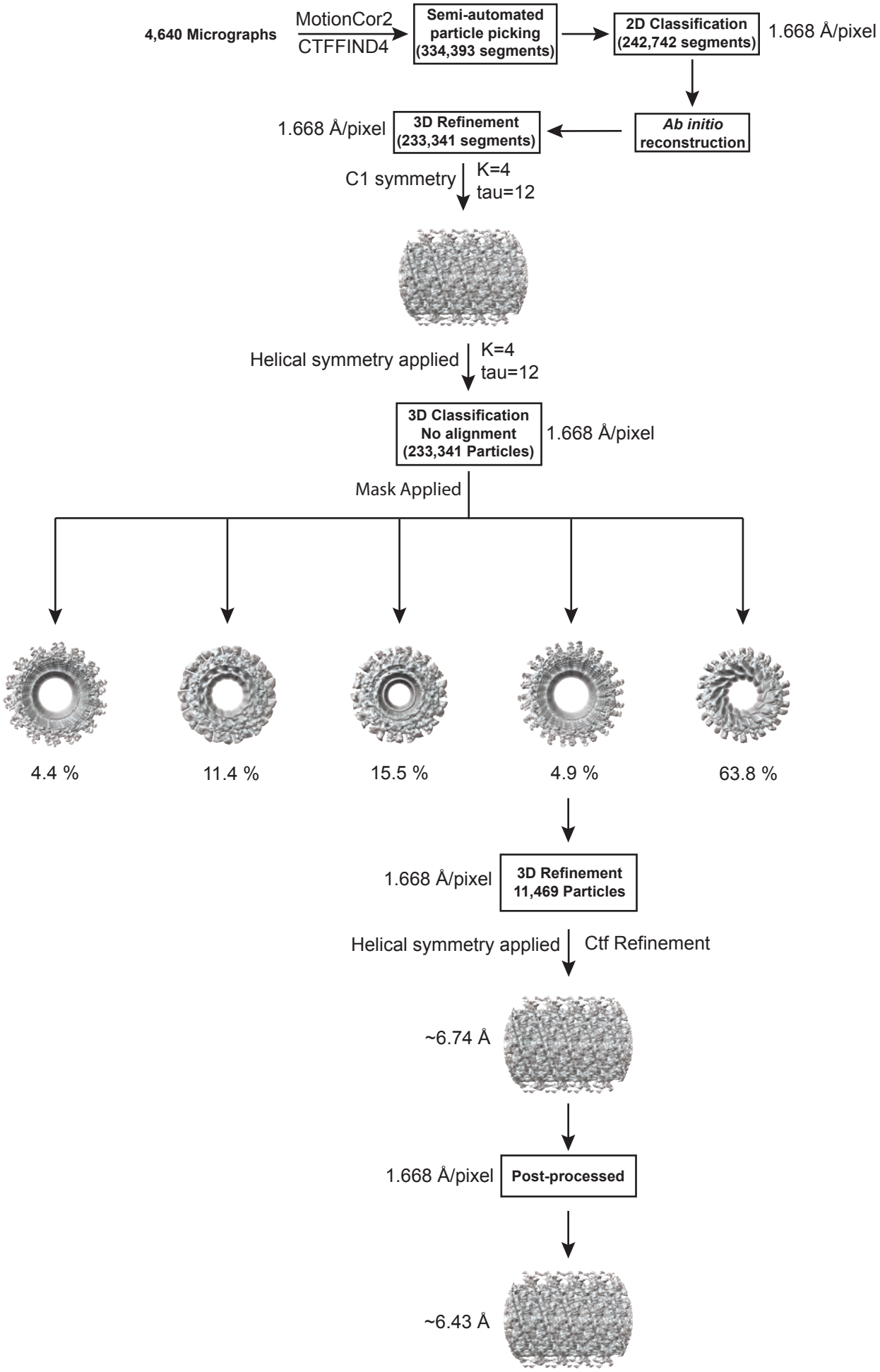

Figure S8

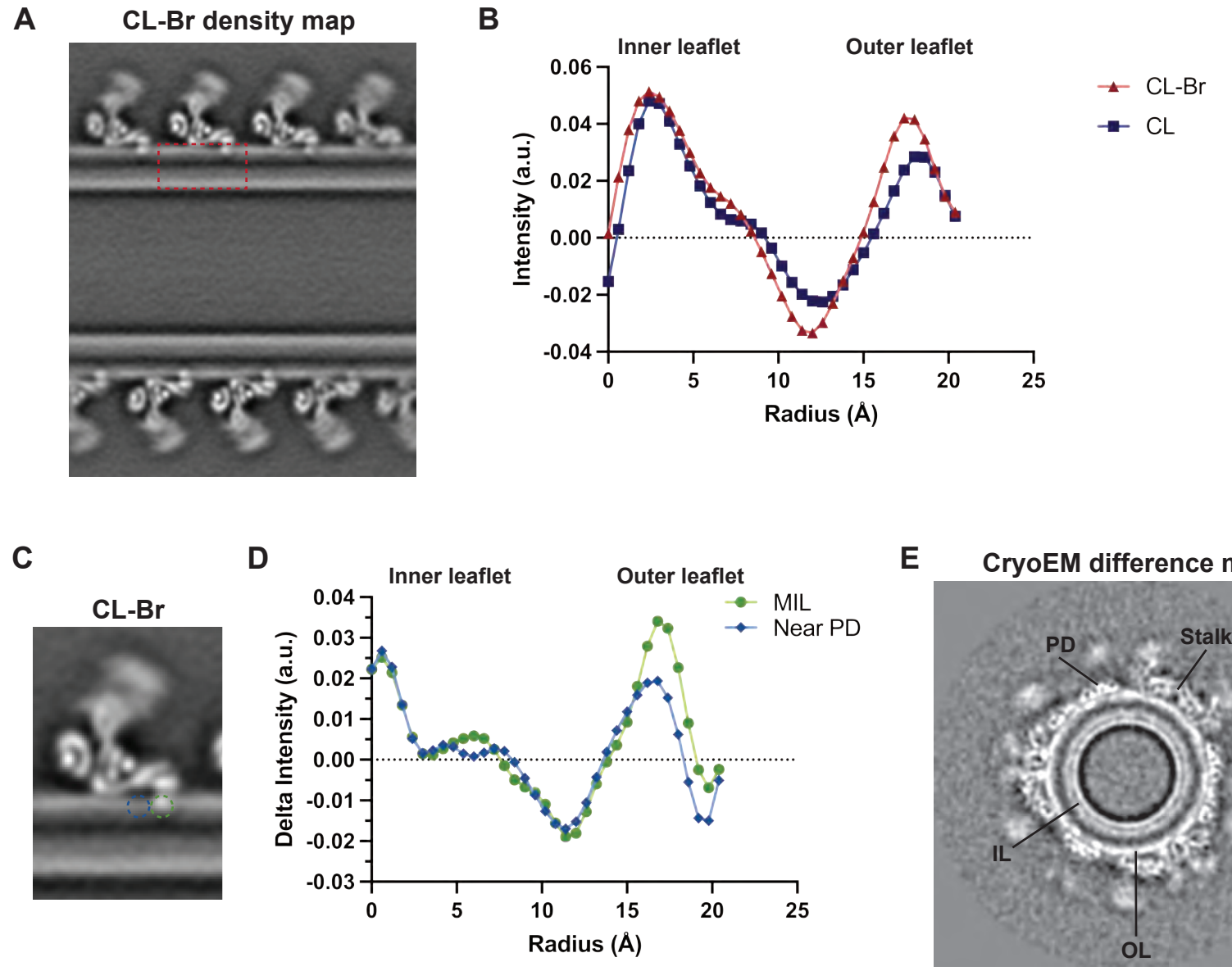

Figure S9

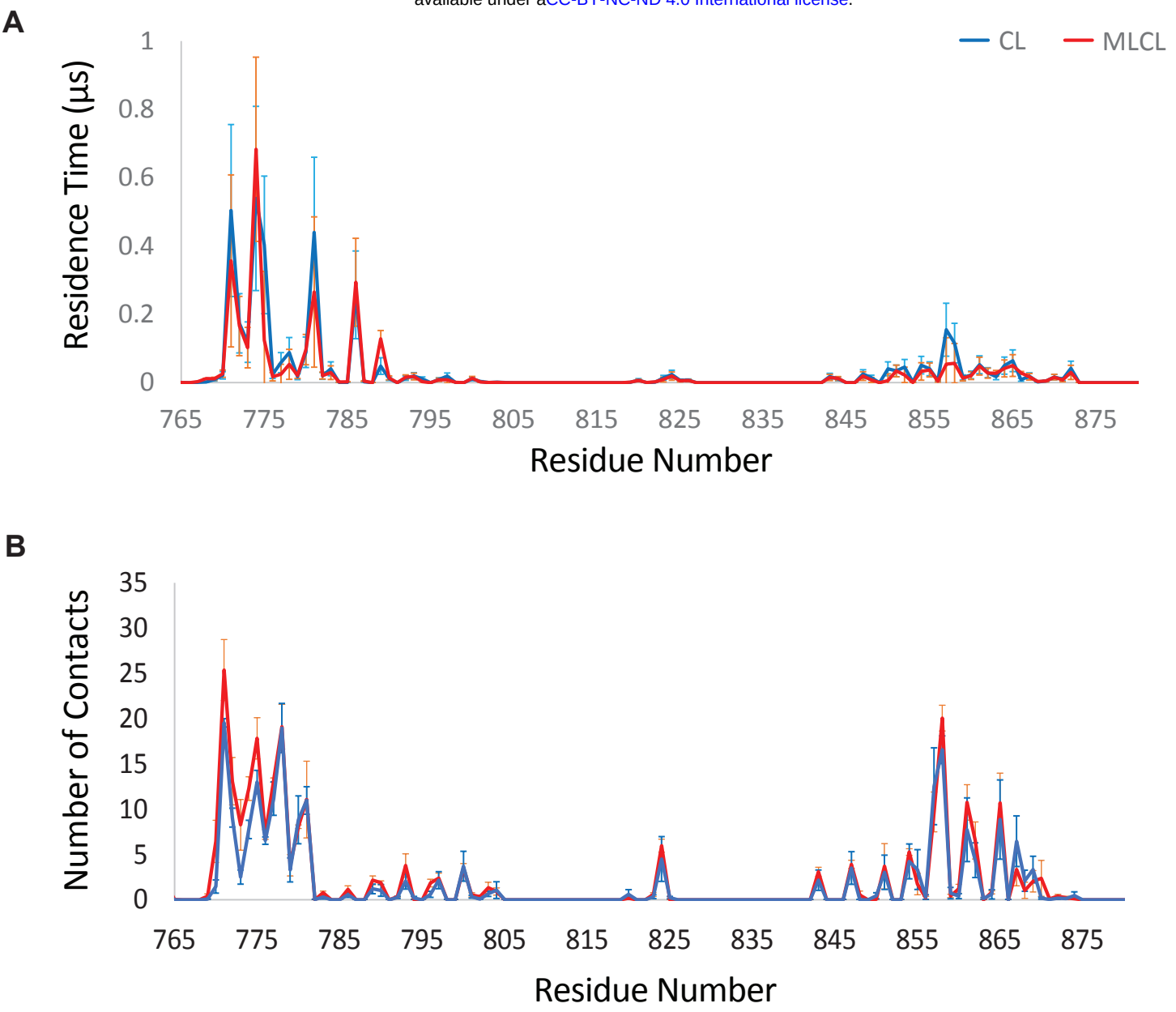

Figure S10

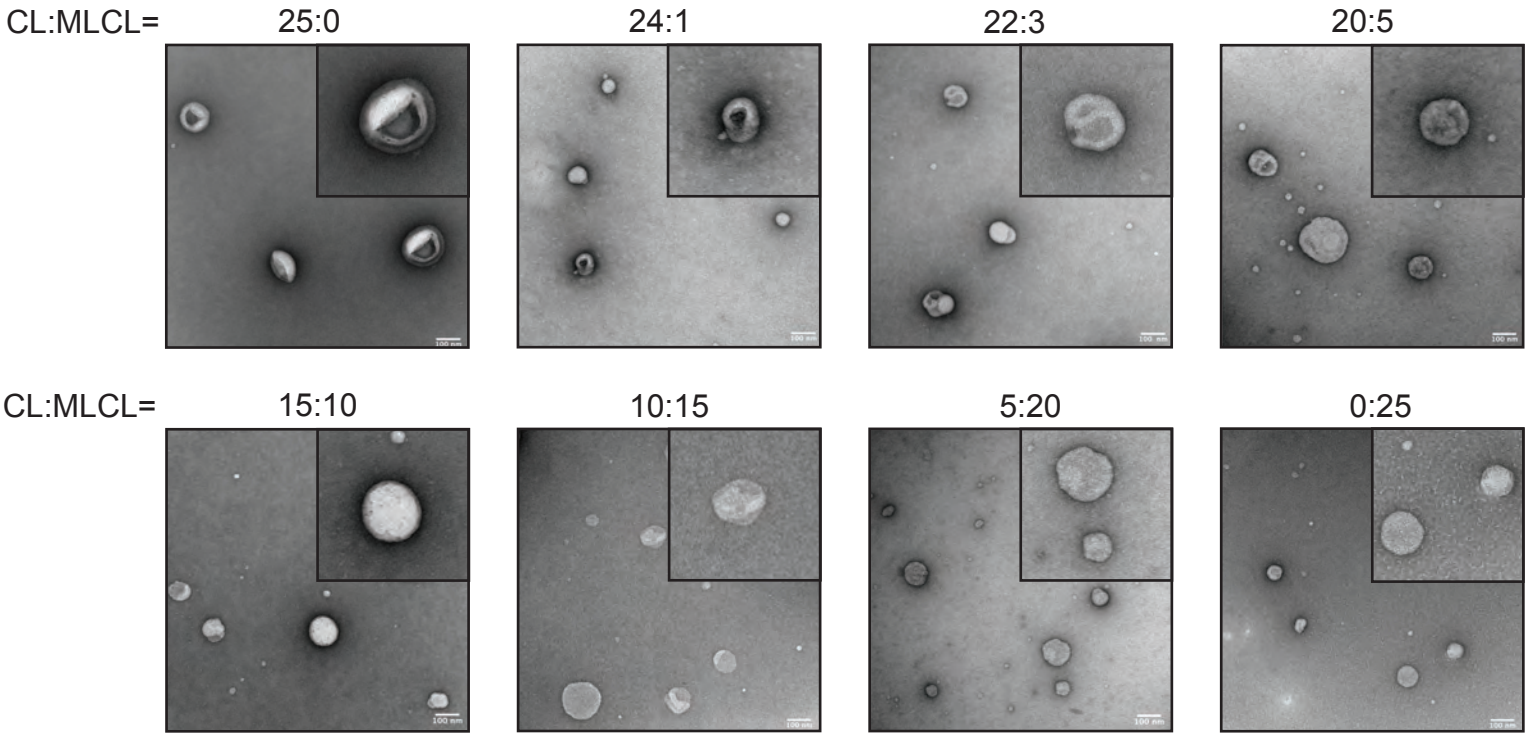

	Human S-OPA1 bound to CL-Br membranes (EMDB-43349)	
Data collection and processing		
Microscope	FEI Titan Krios	
Camera	Gatan K3 Summit	
Magnification	105,000x	
Voltage (kV)	300	
Electron exposure (e^-/ Å^2)	65	
Defocus (um)	0.5 to 1.5	
Pixel Size (Å)	0.834	
Symmetry imposed	Helical	
Micrographs (no.)	4,640	
Initial particle images (no.)	233,341	
Final particle images (no.)	11,469	
Map resolution (Å)	6.4	
FSC threshold	0.143	
Map resolution range (Å)	4.8 to 8.1	4.8 to 8.2
Models Generated (PDB code)	8VLZ	8VM4
Refinement		
Initial model used (PDB code)	8CT1	
Model resolution (Å)	6.4	
FSC threshold	0.143	0.143
Map sharpening B factor (Å^2)	-316.754	
Model composition		
Nonhydrogen atoms	22,723	
Protein residues	2,792	
B factors (Å^2) – min		
Protein	112.87	131.06
R.m.s deviations		
Bond lengths (Å)	0.002	0.002
Bond angles (°)	0.385	0.333
Validation		
MolProbity Score	1.16	1.19
Clashscore	3.68	4.06
Poor rotamers (%)	0.0	0.0
Ramachandran plot		
Favored (%)	99.57	99.57
Allowed (%)	0.43	0.43
Disallowed (%)	0.0	0.0

A

Liposome #	POPC (%)	POPE (%)	L-PI (%)	CL (%)
1	100	0	0	0
2	78	22	0	0
3	70	22	8	0
4	45	22	8	25

B

Liposome #	POPC (%)	POPE (%)	L-PI (%)	CL (%)	MLCL (%)
5	45	22	8	24	1
6	45	22	8	22	3
7	45	22	8	20	5
8	45	22	8	15	10
9	45	22	8	10	15
10	45	22	8	5	20
11	45	22	8	0	25

C

Liposome #	POPC (%)	POPE (%)	L-PI (%)	CL-Br (%)	GalCer (%)
12	45	22	8	25	0
13	0	0	0	10	90